Optical and Electronic Properties of Symmetric InAs/(In,Al,Ga)As/InP Quantum Dots Formed by Ripening in Molecular Beam Epitaxy: A Potential System for Broad-Range Single-Photon Telecom Emitters

P. Holewa,[1,*] M. Gawełczyk,[2,1,‡] A. Maryński,[1,§] P. Wyborski,[1] J.P. Reithmaier,[3] G. Sęk,[1] M. Benyoucef,[3,†] and M. Syperek[1]

[1] *Laboratory for Optical Spectroscopy of Nanostructures, Department of Experimental Physics, Faculty of Fundamental Problems of Technology, Wrocław University of Science and Technology, Wybrzeże Wyspiańskiego 27, Wrocław 50-370, Poland*

[2] *Department of Theoretical Physics, Faculty of Fundamental Problems of Technology, Wrocław University of Science and Technology, Wybrzeże Wyspiańskiego 27, Wrocław 50-370, Poland*

[3] *Institute of Nanostructure Technologies and Analytics (INA), Center for Interdisciplinary Nanostructure Science and Technology (CINSaT), University of Kassel, Heinrich-Plett-Str. 40, Kassel 34132, Germany*

(Received 14 October 2020; accepted 17 November 2020; published 17 December 2020)

We present a detailed experimental optical study supported by theoretical modeling of InAs quantum dots (QDs) embedded in an (In,Al,Ga)As barrier lattice matched to InP(001) grown with the use of a ripening step in molecular beam epitaxy. The method leads to the growth of in-plane symmetric QDs of low surface density, characterized by a multimodal size distribution resulting in a spectrally broad emission in the range of 1.4–2.0 μm, essential for many near-infrared photonic applications. We find that, in contrast to the InAs/InP system, the multimodal distribution results here from a two-monolayer difference in QD height between consecutive families of dots. This may stem from the long-range ordering in the quaternary barrier alloy that stabilizes QD nucleation. Measuring the photoluminescence (PL) lifetime of the spectrally broad emission, we find a nearly dispersionless value of 1.3 ± 0.3 ns. Finally, we examine the temperature dependence of emission characteristics. We underline the impact of localized states in the wetting layer playing the role of carrier reservoir during thermal carrier redistribution. We determine the hole escape to the (In,Al,Ga)As barrier to be a primary PL quenching mechanism in these QDs.

DOI: 10.1103/PhysRevApplied.14.064054

I. INTRODUCTION

Self-assembled InAs quantum dots (QDs) embedded between barriers lattice matched to InP remain attractive candidates for photon emitters in the near-infrared spectral range [1,2]. It is mostly due to vast possibilities to shape their properties and photonic environment to target specific applications ranging from low-threshold lasers to nonclassical photon sources for quantum communication protocols. The latter is especially difficult to achieve, since the typical growth of InAs QDs on the InP substrate by molecular beam epitaxy (MBE) leads to the formation of strongly in-plane asymmetric objects of a significant areal density reaching 10^{10}–10^{11} cm^{-2}. Such high surface coverage prevents sufficient spatial and spectral isolation of individual QDs, while large QD sizes result in an atypically rich and dense optical spectrum unfavorable for single-dot applications [3,4]. The growth process of InAs QDs on an InP(001) substrate and control of their parameters are still challenging and comprise many technological steps and details [5].

Recently, it has been proposed [6,7] to utilize an additional growth step in MBE of InAs QDs on InP(001) that mimics the Ostwald ripening known for the formation of colloidal microcrystals. During the ripening process initially formed QDs decompose, and the material is redistributed between other dots, which typically leads to splitting of the initial QDs size distribution into distinct families. The ripening technique has already been applied to other semiconductor QD systems, such as Ge/Si [8], PbSe/PbTe [9], and InAs/GaAs [10]. In the case of InAs/(In,Al,Ga)As/InP(001) QDs, it has been shown [7] that the mean size of the dots depends on the ripening temperature. These ripening-assisted grown InAs QDs on the InP substrate are particularly promising for quantum information processing as their

*pawel.holewa@pwr.edu.pl

†m.benyoucef@physik.uni-kassel.de

‡Present address: Institute of Physics, Faculty of Physics, Astronomy and Informatics, Nicolaus Copernicus University, Toruń 87-100, Poland.

§Present address: Currently at McKinsey Knowledge Center Poland, 50-141 Wrocław, Poland.

recent development led to demonstrations of single-photon emission at approximately 1.45 μm [6] (the *S* band), coupling to optical modes of photonic crystal microcavities [11], and triggered single-photon emission with high purity [12].

Although some optical experiments on these QDs have already been presented [6,7,11–13], we elaborate here on possible further benefits that come from a single-stage ripening process by pointing at their so-far unexplored and not described application-relevant properties. We focus on: (a) broad spectral coverage of QD emission superimposed with the *S* (1460–1530 nm), *C* (1530–1565 nm), *L* (1565–1625 nm), and *U* (1625–1675 nm) transmission bands of silica fibers, which can be useful for the multiband quantum-secured transmission protocols highly sought for overcrowded long-haul optical networks; (b) the multimodal QD size distribution, simultaneously allowing for better spectral isolation and filtering of single-dot emission, as well as for assuring spatial isolation of a spectrally chosen QD for site-selective engineering of the photonic environment [14] to control the QD emission properties in a future device; (c) thermal stability of emission from QDs, which is important for applications in devices operating at elevated temperatures.

The flexibility in the choice of a quantum emitter from a single wafer in a very broad spectral range covering all the high transmission telecommunication bands can be of practical relevance for certain future applications. It especially concerns all the concepts based on wavelength division multiplexing (WDM), allowing increases in the total transmission rate through the fibers or the optical system efficiency and functionality in analogy to such schemes known from classical communication. For instance, there exist both predictions and experimental demonstrations of the so-called multiuser quantum key distribution employing WDM for quantum networks [15] and showing recently a really impressive increase in the achievable secure key rates [16] and even a practical implementation in a node–free eight-user metropolitan quantum communication network [17]. WDM is also utilized in the on-chip operation using quantum light in photonic integrated circuits [18] for linear optics quantum computation, where the telecom wavelength range is demanded to combine the III-V single-photon emitters with a silicon technological platform. Another branch is gas spectroscopy or the LIDAR-like sensing systems with single-photon emitters in the near infrared considered as prospective and competitive in imaging of gas leaks and dangerous vapors or in performing quantified remote mapping of gases to monitor air quality in agricultural and metropolitan areas [19]. Here, the broad-range selection of the quantum emitters is also profitable to allow detection of many environmentally relevant gasses, such as, e.g., CO_2, N_2O, H_2O, CH_4, having their strong absorption lines in the 1400–1650 nm range. In that context more sophisticated single-photon-based gas detection solutions employing WDM or on-chip spectrometers for, e.g., astronomical observation, spectroscopic imaging, and quantum communications, are also reported [20].

Here, we report on the optical investigations of InAs/(In,Al,Ga)As/InP QDs, which we support by theoretical modeling. We observe the multimodal distribution of QD sizes and explain the emission-energy separation of consecutive QD families by their modeling. With this, we obtain a strong indication that their heights differ by two monolayers (MLs) of InAs. This in turn suggests the presence of long-range ordering of atoms in the barrier alloy that may enhance the reliability of future photonic devices, as it reduces the crystal-lattice free energy [21–23], stabilizing the entire strained QD system.

The detailed goals of this work are to: (i) find the links between QD parameters (height, in-plane size, and chemical composition) and the resulting broad spectral range and other characteristics of emission, (ii) study the character and importance of wetting layer (WL) states, (iii) assess the impact of exciton confinement in a QD on recombination dynamics, (iv) investigate the thermal carrier redistribution processes and optical response of the dots at elevated temperatures. These objectives are achieved by using several complementary spectroscopic tools: modulated reflectivity ($\Delta R/R$), excitation-power-, polarization-, and temperature-dependent photoluminescence (PL), and time-resolved photoluminescence (TRPL), all supported by numerical modeling of exciton states in QDs and WL within the multiband envelope-function $\mathbf{k}\cdot\mathbf{p}$ theory. The collected data and conclusions drawn can trigger the work on such ripening-assisted grown QDs towards unveiling their physical and chemical properties and their use in photonic applications in the near infrared.

II. EXPERIMENTAL AND THEORETICAL METHODOLOGY

In this section we provide details about sample growth, experimental setups, and theoretical framework used to study the optical and electronic properties of the structure.

A. Sample growth

The investigated sample is grown on a (001)-oriented InP substrate using a MBE reactor equipped with two-valved solid-source arsenic and phosphorus cracker cells. The growth sequence starts from a 100-nm-thick InP buffer layer directly deposited on the substrate at 465 °C and followed by a nominally 228-nm-thick $In_{0.53}Al_{0.24}Ga_{0.23}As$ layer lattice matched to InP. A growth interruption lasting for 35 s is introduced to allow for the group-V atoms exchange on the InP/(In,Al,Ga)As interface. Subsequently, the Stranski-Krastanov (SK) growth mode is used to form an initial layer of QDs by deposition of nominally two MLs of InAs at 514 °C with a growth rate of

0.4 ML/s. Following the SK QD formation, the ripening process starts during the reduction of the substrate temperature down to 413 °C with a cooling rate of 30 K/min under As_2 pressure of 6×10^{-6} Torr [7]. After the cooling process, the dots are capped by a nominally 228-nm-thick $In_{0.53}Al_{0.24}Ga_{0.23}As$ layer. During the growth of the cap layer, the substrate temperature is kept at 413 °C for the first 20 nm. Afterwards, it is increased with a rate of 30 K/min up to 514 °C and then kept constant for the remaining layer thickness. More details about the growth procedure can be found in Refs. [6,7].

B. Experimental details

For spectroscopic experiments, the structure is held in a helium closed-cycle refrigerator to allow for the control of the sample temperature in the range of 10–300 K. In the case of PL and TRPL experiments, the sample is excited by a train of approximately 2-ps-long pulses with about a 13.2 ns pulse-to-pulse interval and about a 1.48 eV photon energy. The laser spot is focused to approximately 150 μm in diameter. Emission from the structure is collected in a standard far-field optical setup and dispersed by a 0.3-m-focal-length monochromator. Time-integrated PL spectra are measured in a wide spectral range of 1.2–2.1 μm via the lock-in technique at the reference modulation frequency of 2 kHz, using a thermoelectrically cooled InAs-based single-channel detector. The high-resolution PL is measured in the same setup. However, in this case the excitation and collection of emission are performed through a microscope objective with high numerical aperture NA = 0.65. The laser spot is defined to approximately 2 μm in diameter. A liquid-nitrogen-cooled (In, Ga)As-based linear camera detector registered the high-resolution PL spectrum in the limited spectral range up to 1.65 μm. The TRPL is measured by a time-correlated single-photon counting method. Photons are spectrally filtered by a monochromator and subsequently collected by the NbN superconducting detector. The multichannel event timer is synchronized to the pulse train to produce photon event statistics. The overall temporal resolution of the TRPL setup is approximately 80 ps.

In the $\Delta R/R$ experiment, a halogen lamp is used as a broadband probe beam source. The 630 nm line from a semiconductor diode laser is employed for photomodulation purposes. The 0.3-m-focal-length monochromator dispersed the white light reflected from the sample, the normalized changes of which are measured via the lock-in technique similarly to the PL.

C. Theoretical framework

Initial calculations of single-particle states in the WL and QDs are performed with the commercially available NEXTNANO software [24,25], which utilizes the continuum elasticity model for the strain distribution, and afterwards calculates the electron eigenstates within the eight-band $\mathbf{k}\cdot\mathbf{p}$ method including the strain-driven piezoelectric field. Relevant material parameters are taken from Ref. [26]. The calculations allowed for establishing the bounds for QD parameters (height, lateral dimension, and chemical content) leading to the multimodal energy distribution, analysis of the WL states, and separation between relevant energy states in the investigated structure as an input for discussion on the PL quenching mechanisms.

We then extend the band-structure calculations using a state-of-the-art implementation of the multiband $\mathbf{k}\cdot\mathbf{p}$ method [27,28], including spin-orbit interactions, structural strain, and piezoelectric field up to second-order terms in the strain tensor. Next, exciton states are found within the configuration-interaction approach by diagonalizing the Coulomb and phenomenological electron-hole exchange interactions in the basis of 32×32 electron-hole state configurations, where hole states are obtained by time reversal of valence electron ones. The number of single-particle states included in the calculations is determined on the basis of convergence tests. Then, oscillator strengths and radiative lifetimes for exciton states are obtained within the dipole approximation by computation of matrix elements of the momentum operator $\mathbf{P} = (m_0/\hbar)(\partial H/\partial \mathbf{k})$, where m_0 is the electron mass. The oscillator strength for the ith exciton state composed of a number of electron-hole configurations (single-particle states are labeled by α and β) is then $f_i = 2/(m_0 E_i)|\sum_{\alpha\beta} c_{\alpha\beta}\langle \psi_v^{(\alpha)}|\mathbf{P}|\psi_c^{(\beta)}\rangle|^2$. Finally, we calculate radiative lifetimes, connected with the oscillator strength f by the relation that may be approximately written as $\tau[\mathrm{ns}] = 45(\lambda[\mu\mathrm{m}])^2/nf$, where λ is the emission wavelength and n is the refractive index. The derivation can be found in Ref. [29], while the details of modeling and the parameters taken for the InAs/(In,Al,Ga)As/InP material system can be found in Ref. [30].

III. RESULTS AND DISCUSSION

In this section, we show experimental results supported by theoretical calculations and provide discussion on the properties of the investigated QD structure.

A. Modulated reflectivity and photoluminescence

The measured modulated reflectivity spectrum is plotted with a solid red line in Fig. 1 and shows two noticeable $\Delta R/R$ features settled in the ranges 1.13–1.20 eV and 0.92–0.96 eV, respectively. While the former is attributed to optical absorption involving valence and conduction bands of the (In,Al,Ga)As barrier [31], the latter is tentatively assigned to absorption in the WL. The WL-related feature appears to be constituted of at least two transitions centered at approximately 0.93 and 0.94 eV. The PL spectrum presented as a gray shaded area in Fig. 1

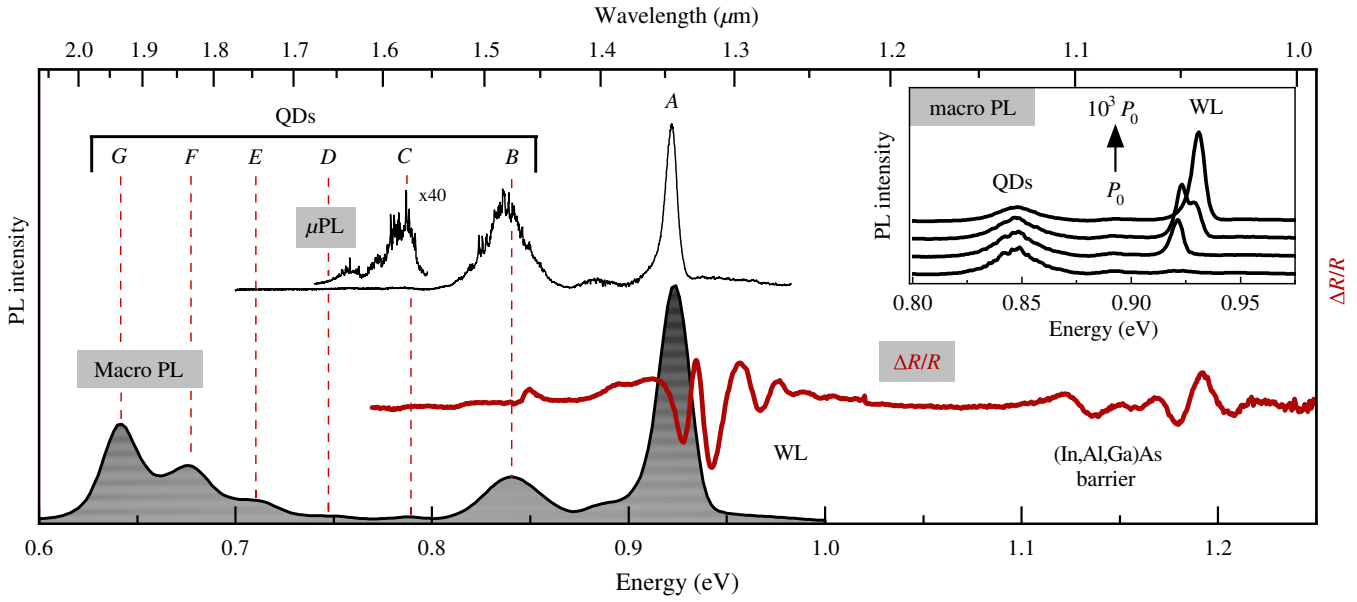

FIG. 1. Photoluminescence (macro PL, gray shaded area), high-resolution PL (μPL, solid black line), and modulated reflectivity ($\Delta R/R$, solid red line) from the structure with QDs at $T = 10$ K. QD-related PL emission bands are labeled B–G, where B denotes remnants of initially grown SK QDs and maxima C–G represent ripening-assisted grown QDs. Inset: power series of macro PL from the B family of QDs and WL.

helps to reveal the nature of both these features. It shows an intensive emission band labeled as A and centered at about 0.93 eV, which overlaps with the low-energy part of the $\Delta R/R$ feature. More interestingly, it changes with increasing optical-pumping power P, as shown in the inset of Fig. 1. For the low pumping power $P = P_0$, band A is centered between 0.92–0.93 eV and shifts towards higher energies with increasing P. We tentatively stated that PL band A and the low-energy $\Delta R/R$ feature are related to optical transitions among the zero-dimensional (0D) localized states in the WL [32–38], whereas the higher-energy $\Delta R/R$ transition involves its 2D band edges. Consequently, the observed evolution of the PL peak A with P can be related to gradual filling of the WL density of states (DOS) starting from its 0D-like tail (0D DOS) and ending in the 2D states. The 0D DOS may originate from an inhomogeneity of the WL due to fluctuation of its thickness and chemical composition, possibly introduced during the ripening stage of the MBE growth. Alternatively, the WL inhomogeneity could be triggered by chemical fluctuations in the (In,Al,Ga)As barrier, as suggested by the spectral smearing of the barrier-related $\Delta R/R$ feature.

The 2D band-edge-related transition in the WL at approximately 0.94 eV allows us to determine the range of possible WL characteristics (composition x of the $In_{0.47x+0.53}Al_{0.24(1-x)}Ga_{0.23(1-x)}As$ alloy and WL thickness d_{WL}). For this purpose, the electronic structure of the WL is calculated, using the NEXTNANO software [24], for d_{WL} varied from 0.9 to 1.5 nm and x from 0.85 to 1. The calculated transition energies are presented in Fig. 2 as a color map, where the two dotted lines distinguish the area of energies corresponding to the WL transition. As we do not expect very strong intermixing, this calculation allows us to determine that the average WL characteristics have to be between four MLs (approximately 1.2 nm) of pure InAs and five MLs (approximately 1.5 nm) of alloy with $x = 0.85$, which resembles the recent transmission electron microscope images of similar QDs [39]. In the latter a rather soft interface with a gradient of composition is

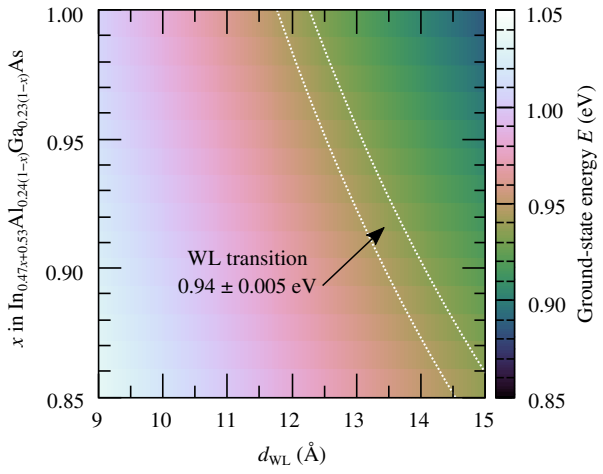

FIG. 2. Color map of the calculated wetting layer ground-state energy as a function of the WL width H (x axis) and material composition (y axis). Dotted white lines mark the energy of the WL transition observed in the $\Delta R/R$ signal.

found. Based on this, in further calculations done for QDs, we take a WL consisting of four MLs of pure InAs and perform Gaussian averaging to simulate the soft interface. Nonetheless, these subtle WL details have in fact only a very minor impact on the QD calculation results presented below.

In Fig. 1 we show also a series of PL peaks below the WL-assigned optical transitions with their positions extending down to approximately 0.6 eV. At least six such bands are resolved and labeled *B*–*G*. These are attributed to emission from QDs with multimodal size distribution formed during the ripening step in the MBE growth. Band *B* has a relatively high intensity compared to bands *C*–*G*, for which the intensity gradually increases. It is reasonable to assume that QDs from family *B* are the remnants of initially grown SK QDs. During the ripening stage, material from partially decomposed SK dots is transferred to other dots, forming the *C*–*G* families. This scenario is supported by previously published structural data [7], where the surface density of the remnants of the initially grown QDs (10^9–10^{10} cm^{-2}) can be comparable to that of newly formed QDs after the ripening stage. Interestingly, for QDs belonging to the *C* family emitting in the telecom spectral range of 1.53–1.63 μm, the surface density seems to be the lowest among all families. Indeed, the μPL spectrum presented in Fig. 1 obtained from the unprocessed sample (without any special patterning of the structure, e.g., mesa etching) shows a discrete spectrum, i.e., sharp and narrow PL lines originating from single QDs. The same is hardly resolvable for QDs in the band *B* and disappears completely for the band *A*, suggesting high areal density of the 0D potential traps in the WL, additionally confirmed by its high PL intensity dominating the emission spectrum.

Bands *B*–*G* originate mostly from ground-state recombination in QDs, rather than from excited states. This conclusion is drawn from the analysis of the pump-fluence-dependent PL presented in Fig. 3(b), which shows a nearly linear increase of the peak intensity with pump fluence across almost three decades. In further analysis of PL spectra we extracted the FWHM, peak position, and peak-to-peak distance (ΔE) between consecutive bands. These are obtained by fitting each PL peak with a Gaussian function. The relevant parameters are shown at the top of Fig. 3(a). PL bands *B*–*G* have the FWHM ranging from 24 to 36 meV, which reveals similar inhomogeneity within each of the QD families that could be in-plane size fluctuations, strain inhomogeneity, and chemical content variation. We observe an expected superlinear decrease in ΔE from approximately 54 meV between peaks *B* and *C* down to approximately 33 meV between *G* and *F* resulting from the quantum size effect. This issue will be further addressed in the theoretical considerations below.

In addition, the angle-resolved linear polarization of PL is presented in Fig. 3(c) for the selected PL bands *A*, *C*, *F*, and *G* to keep the subfigure clear. Surprisingly,

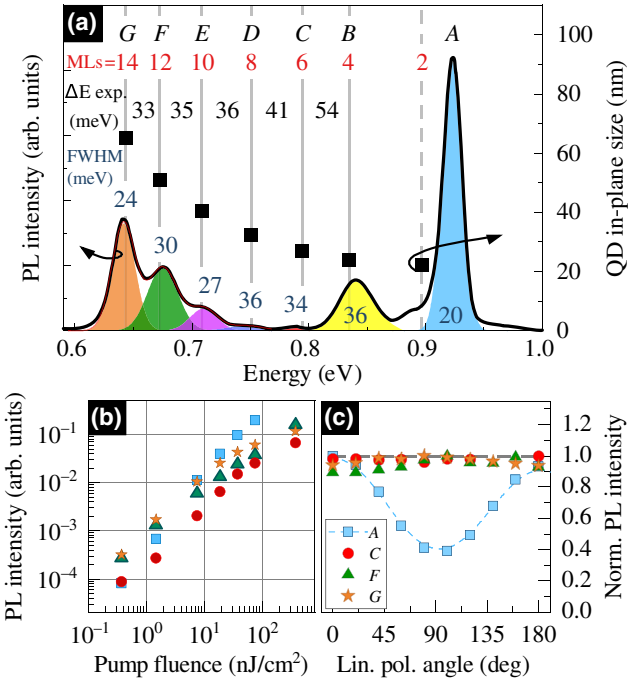

FIG. 3. (a) The PL spectrum (solid black line) at $T = 10$ K with Gaussian fits (color shaded areas for consecutive PL bands). Letters label the peaks; ΔE is the energetic distance between PL bands; FWHM is the full width at half maximum for the peaks. Vertical gray lines indicate energies obtained from numerical calculations for a given QD in-plane size. The dashed gray vertical line indicates potential remnants of initially grown SK QDs with two 2-ML height. Full squares represent the QD in-plane size, determined from the calculations of the ground-state energies. (b) Pump-fluence-dependent PL for selected PL bands: *A* (blue squares), *C* (red circles), *F* (green triangles), and *G* (orange stars). (c) Normalized PL intensity from the selected PL bands in (b), but as a function of the angle of linear polarization with respect to the laboratory frame.

an almost 40% degree of linear polarization (DOLP) is observed for band *A*, whereas for the QD-related bands *C*, *F*, and *G*, the DOLP is negligible, within an experimental accuracy of 5%. The lack of significant DOLP for the QDs can be linked to their high in-plane symmetry that for similar QDs was shown to lead to a negligible fine-structure splitting of the confined exciton states [11,12]. In contrast, high DOLP for band *A* may be related to the built-in optical anisotropy in the WL induced by local strain variations and its anisotropy or chemical disorder at the InAs/(In,Al,Ga)As or (In,Al,Ga)As/InP interfaces.

B. Long-range atom ordering and two-monolayer QD height steps

Previous observations of multimodally distributed InAs QDs embedded directly within the InP barrier were interpreted as resulting from the QD size variation in the form of 1-ML changes in their height between consecutive families [40–42]. A similar observation and interpretation

were also reported for InAs/GaAs QDs [10,43]. This does not seem to apply to the investigated QDs since the 1-ML (approximately 0.3 nm) change in QD height would lead to much smaller energy separation between PL bands than actually observed. Instead, we propose that the height of consecutive QD families changes by 2-ML steps. This hypothesis can find its justification in the expected long-range atom ordering that takes place in the quaternary barrier alloy. The ordering arises spontaneously for a multitude of III-V alloys as the coherent placing of atoms reduces the free energy of the crystal lattice in comparison to a disordered material or to a two-phase alloy [21].

The resulting structure has a modulation of composition along particular crystallographic directions where the elemental cell can be expanded as compared to, e.g., a binary alloy. Therefore, if the barrier above the investigated QD layer is organized in the direction [001] into In-rich and In-poor monolayers alternately then the effective height of a QD may be changed only by an even number of monolayers, i.e. by at least two MLs.

Previous observations of long-range ordering include (Al, Ga)As/GaAs [44], (In, Al)As/InP [45,46], (In, Ga)As/InP(110) [47,48], and (In, As)Sb/InSb(001) [49] heterointerfaces, which establish a background for our conclusion. The most common is the CuPt-type superlattice ($L1_1$ structure) resulting in ordering of cation lattices along the [111] direction [46]. Importantly, it was reported for the (In, Ga, As)P quaternary alloy lattice matched to InP(001) [48,50]. The CuPt-type structure ordering along the [001] direction relevant for this work was modeled [51] and observed for, e.g., bulk (In, Al)As grown on the InP(001) substrate [45,52]. Another, less frequently investigated ordering is the CuAu-I type, which also results in alternating layers along the [001] direction reported for MBE-grown strained (In, Ga)As/(In, Al)As multiple quantum wells on the InP(001) substrate [53]. The atomic ordering was also observed for various III-V and II-VI systems with epitaxial nanostructures [23,54]. For applications, the long-term stability of QDs and their properties is crucial. The size and composition of a highly strained QD after its growth significantly depend on the conditions in the barrier. Thermodynamic calculations suggest that QDs in atomically ordered alloys may be more stable than those grown in random lattices [23]. There are also, e.g., *ab initio* total energy [55,56] and strain energy calculations [23] showing that ordered structures are more stable than random alloys [22]. These results hold for systems with large differences in the lattice constants between the binary constituents; however, the ordering is also observed when this condition is not true. Therefore, other models (kinetic [51] and surface thermodynamic considerations) are proposed to understand this phenomenon for low-mismatch alloys, as in the case of alternating rows of large and small atoms building in along the growth steps (this is the proposed mechanism for the explanation of, e.g., the origin of the ordered CuPt-type structure [57]). These models help to explain the ordering observed for the (Al, Ga)As alloy [44], although AlAs and GaAs have very similar lattice constants.

Although the long-range ordering in III-V ternary and quaternary alloys has been confirmed by crystallographic methods, it has never been observed for the (In,Al,Ga)As quaternary alloy investigated here. Even though our research focuses only on optical properties and does not include the direct investigation of the structural properties, we deduce a similar ordering for (In,Al,Ga)As as has been observed for its constituents [45–48], (In, Ga)As and (In, Al)As, and there is no evident reason that their mixture should organize in a different way. Additionally, there are some premises, e.g., for (Ga, In)As(P) [48], under which ordering in quaternaries may be even more pronounced than in ternaries.

C. Modeling of QDs

The observed multimodal QD emission can be explained based on calculations of the QD ground state as a function of QD parameters (height, lateral dimensions, and chemical composition). The modeled QD geometry is a truncated pyramid with a square at the base and an angle between the side facets and the base of 25°, in accordance with the structural studies of QDs grown under similar conditions [39]. The dot is settled on a 4-ML-thick WL, and the barrier material is $In_{0.53}Ga_{0.23}Al_{0.24}As$.

We begin with two initial series of single-particle calculations, in which we take almost pure InAs ($In_{0.95}Al_{0.025}Ga_{0.025}As$) in the WL and a purely InAs QD with height varying by one ML and two fixed in-plane sizes, $L = 25$ nm and $L = 45$ nm, plotted in Fig. 4 with blue squares and diamonds, respectively. These results are compared with the experimental data plotted with black squares at 2-ML height steps and with gray squares at 1-ML steps. While the qualitative agreement is very weak, one may note that the assumption on the 2-ML QD height variation, and thus the presence of long-range ordering and the resulting enhanced stability of QDs, is correct here. Additionally, with a dotted green line we plot the ground-state energy for the limit of $L \to \infty$, i.e., for a quantum well (QW) as high as the studied QDs. The experimental data plotted assuming 1-ML steps (gray squares) is so steep that it even crosses this line, which makes it nonphysical, as it implies QDs having lower energy than for the QW. Thus, at this point we establish that the *G* family with emission around 0.65 eV is assigned as having $H = 14$ MLs, while $H = 4$ MLs characterizes the *B* family centered near 0.84 eV. Within this assumption, the smallest dots having 2-ML height should emit near 0.89 eV. Indeed, at this energy the PL spectra in Figs. 1 and 3 (vertical dashed gray line) reveal a PL band of low intensity overlapping with

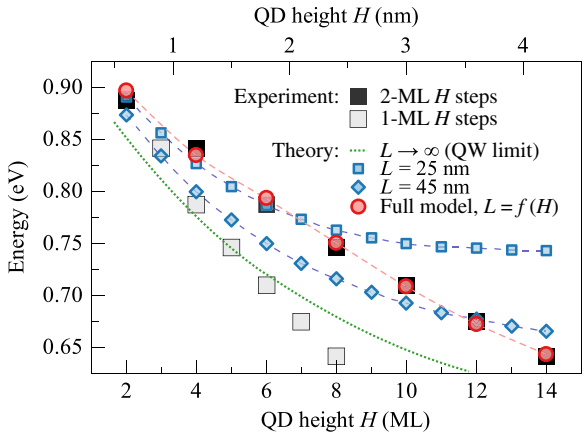

FIG. 4. Comparison of observed QD emission energies, plotted assuming 2-ML (black squares) and 1-ML (gray squares) steps in the QD heights, with trends calculated in a simple model for QDs with $L = 25$ nm (blue squares) and $L = 45$ nm (blue diamonds), as well as in the full model including the exciton binding energy and varying dependence $L = f(H)$. The dotted green line shows energy calculated for a quantum well. The height H is measured from the top of the WL.

tails of bands A and B, which thus comes from the 2-ML height QDs.

For two probe cases related to fixed L, the calculated ground-state energies as a function of H deviate from the postulated trend especially for larger heights. The obtained energy change saturates for large H, as predicted by the H^{-2} dependence. Therefore, to obtain agreement between the experimental and theoretical points, we need to introduce an additional, nonlinear dependence that relates H with L, which we presented in Fig. 3. It allowed us to achieve good qualitative agreement; the respective theoretical values are plotted with red circles. This final series of calculations is performed in an extended model taking into account the electron-hole Coulomb interaction and soft material interfaces. Starting with nominally clean InAs inside the WL and QDs, Gaussian averaging (with $\sigma = 0.3$ nm) of the material profile is used to simulate material intermixing at interfaces. QDs of height from 2 to 14 MLs are simulated, with the in-plane size varied in the range of $L = 25$–70 nm. The resultant dependence of the ground-state energy on these dimensions is very smooth, thus allowing for extraction of the $L = f(H)$ dependence that is then fit to the experimental values. Finally, this nonlinear dependence introduced into QD modeling resulted in very good agreement between the calculated energies and the positions of the PL peaks (see the red circles in Fig. 4).

The introduction of variable L might suggest that in principle the experimental data could also be reproduced assuming 1-ML height steps, by using a strong enough dependence of L on H. This is however not the case. As mentioned above, the 1-ML-stepped experimental data cross the theoretical result obtained for a quantum well, which means that the hypothetical $L(H)$ dependence is divergent. Thus, such a sequence of ground-state energies could not be obtained for QDs varying in height by a single ML.

D. Carrier dynamics

The theoretical calculation of excitonic states in QDs also allowed us to determine the exciton recombination dynamics, presented as a solid red line in Fig. 5. The result of the comparison with the experimental values may shed some light on the correctness of the assumptions made and the legitimacy of using a specific set of QD structural parameters.

The TRPL experiment is performed at $T = 10$ K. The PL decay curves measured at each of the respective PL peaks shown in Fig. 3(a) are analyzed using the PTI FelixGX software by Photon Technology International. Using the maximal entropy method (MEM) [58,59], the PL lifetimes are extracted without initial knowledge or assumptions on the number of underlying processes. Because of this, the MEM has proved effective in reconstructing decays consisting of several exponential components [60]. In this approach, we obtain a distribution of times of nonzero width, which results from the incomplete (noisy) information. The reconstruction formula is

$$I(t) = I(0) \sum_{i=1}^{N} A_i \exp\left(-\frac{t}{\tau_i}\right), \tag{1}$$

where N is the number of components in the quasicontinuous distribution of lifetimes describing the decay, and coefficients A_i are the corresponding amplitudes. If the distribution is a set of well-resolved peaks, it is valid to treat their means as single representative lifetimes. Such averages are plotted with circles in Fig. 5.

The PL lifetimes obtained for QD families B–F (1.4 ± 0.2, 1.5 ± 0.2, 1.2 ± 0.2, and 1.1 ± 0.2 ns, respectively) are similar and, as their variation is on the level of

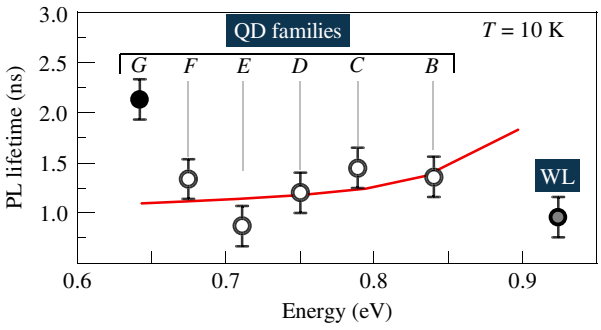

FIG. 5. PL lifetimes at $T = 10$ K for different families of ripening-assisted grown InAs/(In,Al,Ga)As/InP(001) QDs (PL bands B–G) and the WL (PL band A). The solid red line is a calculated trend for the PL lifetime.

the experimental uncertainty, no clear trend can be determined. These overall values that average to 1.3 ± 0.3 ns agree well with those obtained theoretically. In theory, a noticeable increasing trend is present, due to effectively weaker (relative to single-particle level spacing) electron-hole Coulomb interaction in smaller QDs. However, the uncertainty of experimental values does not allow this result to be verified. At the emission energy of 0.84 eV, a similar PL lifetime of approximately 1.65 ns has been obtained for slightly in-plane asymmetric SK InAs/(In,Al,Ga)As/InP(001) QDs [31]. For highly asymmetric confining potentials like those in InAs/(In,Al,Ga)As/InP(001) quantum dashes, the PL lifetime consists of two short and long components [30]. Nevertheless, the average PL lifetime of 1.45–1.8 ns is comparable to that obtained here, and indicates the main influence of the exciton confinement regime on the observed PL dynamics.

A significantly different value is obtained for family *G*, where the analysis yields a PL lifetime of 2.0 ± 0.2 ns. This family also shows a different PL quenching characteristic than other families, as discussed in the next section, which may suggest a much different exciton confinement nature reflected in a much longer PL decay time.

Finally, the observed long PL decay time of 0.9 ± 0.2 ns for the 0D WL states represented by PL band peak *A* at approximately 0.93 eV confirms the localized nature of the states [38] since the lifetime of excitons confined in the 2D WL is expected to be significantly shorter.

E. Temperature-dependent photoluminescence

In this section, we describe temperature-dependent PL that provides information on the carrier confinement parameters in the WL and QDs and the thermal carrier redistribution processes involving 0D and 2D states in this system.

First, the analysis focuses on the thermal shift of the PL peak energy presented in Fig. 6(a). The shift is compared to the well-known Varshni relation for the temperature dependence of the energy gap for a bulk InAs material [61]:

$$E_g(T) = E_g(0) - \frac{\alpha T^2}{T + \beta}. \tag{2}$$

Here $E_g(0)$ is the estimated transition energy at $T = 0$ K, with $\alpha = 2.76 \times 10^{-4}$ eV/K^2 and $\beta = 93$ K the parameters for InAs.

From Fig. 6(a) we infer that, for PL band *A* (blue circles), the peak energy follows the Varshni relation (solid blue line) only at elevated temperatures. At $T < 120$ K, the peak position remains nearly *T* independent or slightly drops when *T* decreases. The effect reminds the so-called "S-shape" function for a QW [62,63]. In this case, photoinjected carriers populate 0D-like states residing below the QW's mobility edge (2D states) and the resultant emission under low photoexcitation conditions involves the localized states only. The WL can be considered as a QW with additional localization potentials that come from, e.g., fluctuations of its width and chemical content, as well as variations of local strain. However, the optical response from the 2D WL states should be present: (i) in the PL spectrum, once the 0D states are fully occupied, preventing the carrier transfer process from 2D to 0D WL states, or (ii) in the $\Delta R/R$ trace, where all the 2D states with a large transition oscillator strength are accessible in the optical absorption process. Both are observed experimentally among the registered data set. The extrapolation of the Varshni trend to low temperatures predicts the optical response involving 2D WL states to be observed at approximately 0.94 eV. While the inset of Fig. 1 shows the shift of PL band *A* towards the predicted energy range with increasing excitation power, the $\Delta R/R$ experiment presented in Fig. 1 reveals the highly intensive feature at 0.94 eV, identified as the optical absorption process involving 2D WL states. The energy distance between PL band *A* and

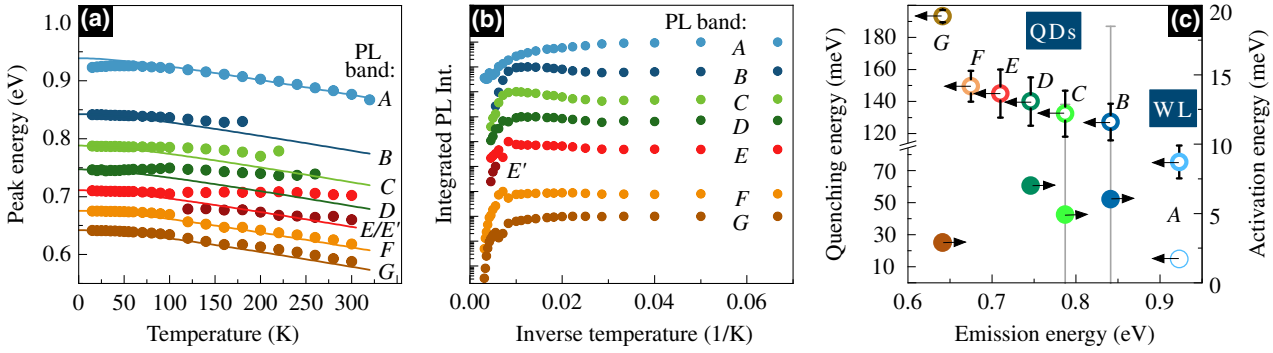

FIG. 6. Analysis of temperature-dependent PL spectra: (a) PL band peak energy, (b) integrated PL intensity, (c) activation (closed circles) and quenching (open circles) energies for the emission bands taken from the Arrhenius fit.

the 2D WL is approximately 10 meV at $T = 10$ K, which may serve as a rough estimate of the carrier localization energy. These observations confirm the existence of 0D WL states able to localize carriers at low T and suggest their impact on the thermal carrier redistribution process in the structure. A similar issue has previously been studied for (In,Ga)As/GaAs QDs [38].

The temperature dependence of QD-related PL bands *B*–*G* is different from that observed for the WL emission. At $T < 40$ K, the peak energy follows the Varshni trend. However, with increasing T, the redshift is either stopped (bands *B*–*E*) or weakened (bands *F* and *G*). This so-called anomalous energy shift is only partially caused by the bandgap reduction of the QD material [64]. It is predominantly related to the migration of carriers between different QD families and within each of them, as well as involving an exchange of carriers with the WL reservoir. During the thermally activated redistribution, carriers can be captured by QDs characterized by high emission energy. Therefore, the high-energy tails of QD size distributions in each of the families become optically active, shifting the PL-band peak energy towards higher energies, thus compensating for the effect of the thermal bandgap reduction [64].

The analysis of the temperature-dependent PL intensity presented in Fig. 6(b) provides further information about the carrier redistribution in the investigated structure. Each data set is fitted with the Arrhenius-type formula

$$I(T) = \frac{I_0}{1 + \sum_i B_i \exp(-E_i/k_B T)}, \tag{3}$$

where E_i is the average activation energy (or PL quenching energy) and B_i is the amplitude of the activation (PL quenching) process. The respective energies are summarized in Fig. 6(c).

For the already discussed PL band *A* originating from the 0D WL states overlapping with 2D WL states, the PL intensity is thermally quenched, characterized by two energies of 16 ± 2 and 75 ± 22 meV, represented by open blue circles in Fig. 6(c) at approximately 0.93 eV. The lower energy is close to the estimated energy of the additional localization in the WL, most probably caused by the fluctuations in the chemical content and/or the WL width variations. Note that these two do not have to match, as the latter is a difference between exciton levels in the WL and in an additional potential trap, while the former is composed of such a difference for just one of the carriers (most probably the hole) and exciton binding energy. Since the PL quenching is rather weak in the low-T range, most of the exciton population is trapped back to the 0D WL states and recombines there, while only a small exciton population feeds QDs. In the range of higher temperatures more complex PL quenching processes occur. When the thermal energy is larger, the WL reservoir is depopulated by the carrier capture in QDs, and at the same time, reactivated carriers from QDs supply the WL reservoir. Against this background, the escape of holes from the WL to the barrier seems to be the most important process, as the higher quenching-related energy corresponds well to the calculated difference in hole levels plus the exciton binding energy in the WL.

Prior to the discussion on the characteristic PL quenching and activation energies for QDs, it is justified to assume that in the low-T limit free carrier migration is negligible. This comes from the calculated electron-hole Coulomb correlation energy between approximately 9.5 meV for 14-ML-high QDs and approximately 20 meV for the flattest ones, which corresponds to $T \sim 110$–235 K. At higher temperatures, electrons and holes can escape from the confining potential with characteristic activation energies composed of the energy distance to WL states (δ_e, δ_h) or barrier band edges (Δ_e, Δ_h), in which we also include the exciton binding energy (E_b), as the exciton has to dissociate.

Let us now refocus on the T-dependent PL intensity from QDs. For families *B*–*D*, an enhancement is first observed, followed by a decrease of intensity at elevated temperatures. The extracted activation energy connected with this enhancement is approximately 6 meV with variation within the uncertainty bounds, as depicted with full circles in Fig. 6(c). This is close to the determined PL quenching energy for the 0D WL states, suggesting that QDs may acquire excitons released from the WL already at low T. However, this feeding process competes with the thermal escape of carriers at elevated temperatures. Energies connected with quenching of PL from QD families are depicted with open circles in Fig. 6(c), with values varying between 127 ± 11 and 150 ± 10 meV. As could be expected, a monotonic increase of quenching-related energies with rising QD size (families *B*–*F*) is present, as the localized states are sunk deeper into a wider potential.

To propose a scenario underlying the carrier activation process, one can compare the obtained PL quenching energies with calculated energy distances between the lowest single-particle electron (e_1) and hole (h_1) states confined in a dot and respective 2D WL ground states (e_{WL}, h_{WL}) or the (In,Al,Ga)As barrier (e_{bulk}, h_{bulk}). Results are presented in Fig. 7(a) together with a sketch of the confining potential in a QD and the WL in Fig. 7(b). Note that all the calculated energy differences $\delta_e = e_{\mathrm{WL}} - e_1 + E_b$, $\delta_h = h_1 - h_{\mathrm{WL}} + E_b$, $\Delta_e = e_{\mathrm{bulk}} - e_1 + E_b$, $\Delta_h = h_1 - h_{\mathrm{bulk}} + E_b$ include the electron-hole interaction energy, as discussed above. Additionally, with stars we also plot the calculated energy of exciton extraction to the WL, in which the difference between 0D and 2D exciton binding energies is taken into account.

From Fig. 7(a), note that extraction of a single electron from a dot to the barrier cannot be responsible for the PL quenching in the considered T range since the Δ_e (green

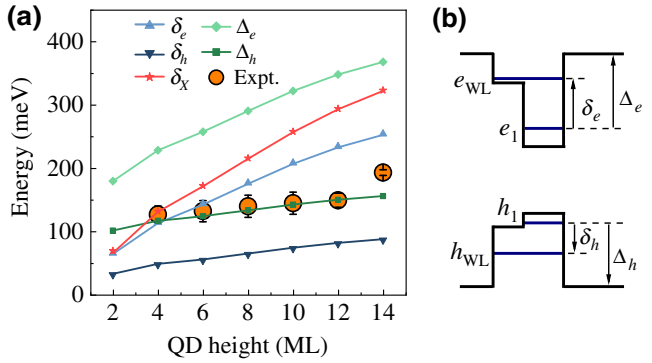

FIG. 7. (a) Comparison between experimentally obtained PL quenching energies (orange circles) and calculated energy distances between single-particle electron (e_1) and hole (h_1) ground states confined in a QD and (i) 2D WL electron (e_{WL}) and hole (h_{WL}) states, with $\delta_e = e_{WL} - e_1 + E_b$ and $\delta_h = h_1 - h_{WL} + E_b$, and (ii) the (In,Al,Ga)As barrier, where Δ_e and Δ_h are the distances from QD states to the conduction- and valence-band edges in the barrier, respectively. Here $\delta_X = \delta_e + \delta_h + E_b$ is sum of energy required to dissolve the exciton (E_b) and excite both carriers to the WL (δ_e, δ_h). (b) Energy diagram of the confinement potential for the system with a QD and the WL.

diamonds) is far above the obtained PL quenching energies (orange circles). From the primary PL quenching mechanism, we can also exclude hole escape from a dot to the WL. The calculated energy distance δ_h for the dots (blue down triangles) is too small to match the PL quenching energy. Note, however, that despite the relatively small energy necessary to eject a hole to the WL, the inverse process of fast hole relaxation mechanisms back to a QD at low T may lead to the absence of quenching related to such energies.

For small QDs, with $H \leq 6$ MLs, at least three PL quenching mechanisms can be considered: (i) the one related to single-electron escape to the WL [blue up triangles in Fig. 7(a)], (ii) single-hole escape to the barrier (green squares), and (iii) whole exciton extraction to the WL (red stars). In all these cases the calculated energy distances closely or perfectly fit the respective PL quenching energies.

For large QDs, with $H > 6$ MLs, the dominant PL quenching mechanism seems to be related to single-hole escape to the barrier as the calculated energy distance Δ_h perfectly matches the quenching energy. Since the hole extraction to the barrier is also present for small QDs, we can conclude that it can be the primary mechanism for the PL quenching in the investigated QDs.

Finally, we comment on the observed anomalies in the temperature dependence of PL from the investigated structure. At $T > 125$ K, the PL spectrum is enriched by the appearance of the PL band labeled E' between previously identified bands E and F. Temperature dependence of the E' band is presented in Fig. 6(a); however, the fitting procedure did not allow for a precise determination of changes in the band intensity due to its substantial overlap with bands E and F. The origin of the band is unknown; it could be related to another family of QDs that is split off from families E and F. Another anomaly is related to the observation of two quenching energies for band G. While the higher one, 193 ± 5 meV, is in agreement with the abovementioned general scenario for QDs, the lower one, 25 ± 5 meV, suggests the existence of another nonradiative relaxation channel that we could not identify.

IV. SUMMARY

In conclusion, we perform detailed optical studies of InAs/(In,Al,Ga)As/InP(001) QDs grown by MBE employing the ripening-assisted scheme. QDs emit in the 1.4–2 μm spectral range, which places them among attractive solutions for photonic applications in the near infrared. We study a multimodal emission from QDs, which reveals their grouping into at least six families according to their height. Based on the quantitative agreement between our theoretical calculations and experimental data, we show that the dots belonging to the consecutive families differ by two material monolayers in QD height, contrarily to 1-ML steps typically observed for InAs/InP QDs made of binary alloys. We suggest that this may stem from crystallographic long-range ordering in the quaternary (In,Al,Ga)As barrier alloy that stabilises the growth of InAs QDs. Because of the minimization of the crystal lattice free energy by atomic ordering, QDs in such systems should be characterized by higher long-term stability in comparison to those embedded in alloys without ordering, which is also beneficial for future applications. We also find that QDs from consecutive families differ significantly in lateral dimensions spanning the 24–65 nm range of in-plane sizes. Such geometries allow us to calculate the relatively short PL lifetimes monotonically decreasing from approximately 1.4 ns for flat dots to approximately 1.1 ns for higher ones, which agrees with the mean trend from experimental data. Observation of a single-exponential decay and negligible linear polarization of PL from QDs suggest their high in-plane symmetry. Finally, we observe a thermal carrier redistribution process, in which localized states in the WL play the role of carrier reservoir, feeding the QDs at elevated temperatures. Based on the comparison of calculated energy splittings between carrier states in the dots, the wetting layer, and in the barrier with the experimental data, we determine that the dominant PL quenching mechanism is the escape of holes to the barrier.

ACKNOWLEDGMENTS

M.G., G.S., and M.S. acknowledge financial support from the National Science Centre (Poland) under Grant

No. 2014/14/M/ST3/00821. P.H. acknowledges financial support from the Polish budgetary funds for science in 2018–2020 via the "Diamond Grant" program (Ministry for Science and Higher Education, Grant No. DI 2017 011747) and from the National Science Centre (Poland) under the Etiuda 8 Grant No. 2020/36/T/ST5/00511. A.M. acknowledges financial support from the National Science Centre (Poland) grant Preludium 8 (project No. 2014/15/N/ST7/04708). This work is also financially supported by the BMBF Project (Q.Link.X) and DFG (DeLiCom). We thank Krzysztof Gawarecki for sharing his implementation of the $\mathbf{k}\cdot\mathbf{p}$ method, Janusz Andrzejewski for discussions of the calculation results, and Matusala Yacob for his assistance in the MBE growth process.

[1] P. Senellart, G. Solomon, and A. White, High-performance semiconductor quantum-dot single-photon sources, Nat. Nanotechnol. **12**, 1026 (2017).

[2] S. Buckley, K. Rivoire, and J. Vučković, Engineered quantum dot single-photon sources, Rep. Prog. Phys. **75**, 126503 (2012).

[3] M. Gawełczyk, Excitons in asymmetric nanostructures: Confinement regime, Acta Phys. Pol. A **134**, 930 (2018).

[4] M. Gawełczyk, P. Wyborski, P. Podemski, J. P. Reithmaier, S. Höfling, and G. Sęk, Excited states of neutral and charged excitons in single strongly asymmetric InP-based nanostructures emitting in the telecom C band, Phys. Rev. B **100**, 241304 (2019).

[5] M. Z. M. Khan, T. K. Ng, and B. S. Ooi, Self-assembled InAs/InP quantum dots and quantum dashes: Material structures and devices, Prog. Quantum. Electron. **38**, 237 (2014).

[6] M. Benyoucef, M. Yacob, J. P. Reithmaier, J. Kettler, and P. Michler, Telecom-wavelength (1.5 μm) single-photon emission from InP-based quantum dots, Appl. Phys. Lett. **103**, 162101 (2013).

[7] M. Yacob, J. P. Reithmaier, and M. Benyoucef, Low-density InP-based quantum dots emitting around the 1.5 μm telecom wavelength range, Appl. Phys. Lett. **104**, 022113 (2014).

[8] F. M. Ross, J. Tersoff, and R. M. Tromp, Coarsening of Self-Assembled Ge Quantum Dots on Si(001), Phys. Rev. Lett. **80**, 984 (1998).

[9] A. Raab and G. Springholz, Oswald ripening and shape transitions of self-assembled PbSe quantum dots on PbTe (111) during annealing, Appl. Phys. Lett. **77**, 2991 (2000).

[10] K. Pötschke, L. Müller-Kirsch, R. Heitz, R. L. Sellin, U. W. Pohl, D. Bimberg, N. Zakharov, and P. Werner, Ripening of self-organized InAs quantum dots, Phys. E Low-Dimens. Syst. Nanostruct. **21**, 606 (2004).

[11] A. Kors, K. Fuchs, M. Yacob, J. P. Reithmaier, and M. Benyoucef, Telecom wavelength emitting single quantum dots coupled to InP-based photonic crystal microcavities, Appl. Phys. Lett. **110**, 031101 (2017).

[12] A. Musiał, P. Holewa, P. Wyborski, M. Syperek, A. Kors, J. P. Reithmaier, G. Sęk, and M. Benyoucef, High-purity triggered single-photon emission from symmetric single InAs/InP quantum dots around the telecom C-band window, Adv. Quantum Technol. **3**, 1900082 (2019).

[13] A. Kors, J. P. Reithmaier, and M. Benyoucef, Telecom wavelength single quantum dots with very small excitonic fine-structure splitting, Appl. Phys. Lett. **112**, 172102 (2018).

[14] L. Sapienza, M. Davanço, A. Badolato, and K. Srinivasan, Nanoscale optical positioning of single quantum dots for bright and pure single-photon emission, Nat. Commun. **6**, 7833 (2015).

[15] G. Brassard, F. Bussieres, N. Godbout, and S. Lacroix, in *Applications of Photonic Technology 6*, edited by R. A. Lessard and G. A. Lampropoulos (SPIE, Quebec City, Québec, Canada, 2003).

[16] T. A. Eriksson, T. Hirano, B. J. Puttnam, G. Rademacher, R. S. Luís, M. Fujiwara, R. Namiki, Y. Awaji, M. Takeoka, N. Wada, and M. Sasaki, Wavelength division multiplexing of continuous variable quantum key distribution and 18.3 Tbit/s data channels, Commun. Phys. **2**, 9 (2019).

[17] S. K. Joshi, D. Aktas, S. Wengerowsky, M. Lončarić, S. P. Neumann, B. Liu, T. Scheidl, G. C. Lorenzo, Ž. Samec, L. Kling, A. Qiu, M. Razavi, M. Stipčević, J. G. Rarity, and R. Ursin, A trusted node–free eight-user metropolitan quantum communication network, Sci. Adv. **6**, eaba0959 (2020).

[18] A. W. Elshaari, I. E. Zadeh, A. Fognini, M. E. Reimer, D. Dalacu, P. J. Poole, V. Zwiller, and K. D. Jöns, On-chip single photon filtering and multiplexing in hybrid quantum photonic circuits, Nat. Commun. **8**, 379 (2017).

[19] https://www.idquantique.com/.

[20] R. Cheng, C.-L. Zou, X. Guo, S. Wang, X. Han, and H. X. Tang, Broadband on-chip single-photon spectrometer, Nat. Commun. **10**, 4104 (2019).

[21] G. B. Stringfellow, Atomic ordering in III/V semiconductor alloys, J. Vac. Sci. Technol. B **9**, 2182 (1991).

[22] G. Stringfellow, Ordered structures and metastable alloys grown by OMVPE, J. Cryst. Growth **98**, 108 (1989).

[23] P. Moeck, Epitaxial and endotaxial semiconductor quantum dots: A brief review on atomic ordering and the void-mediated formation mechanism, Nonlinear Anal. Theory Methods Appl. **63**, e1311 (2005).

[24] The release date is October 31, 2018.

[25] S. Birner, T. Zibold, T. Andlauer, T. Kubis, M. Sabathil, A. Trellakis, and P. Vogl, nextnano: General purpose 3-D simulations, IEEE Trans. Electron Devices **54**, 2137 (2007).

[26] I. Vurgaftman, J. R. Meyer, and L. R. Ram-Mohan, Band parameters for III–V compound semiconductors and their alloys, J. Appl. Phys. **89**, 5815 (2001).

[27] K. Gawarecki, P. Machnikowski, and T. Kuhn, Electron states in a double quantum dot with broken axial symmetry, Phys. Rev. B **90**, 085437 (2014).

[28] K. Gawarecki, Spin-orbit coupling and magnetic-field dependence of carrier states in a self-assembled quantum dot, Phys. Rev. B **97**, 235408 (2018).

[29] K. Karrai and R. J. Warburton, Optical transmission and reflection spectroscopy of single quantum dots, Superlattices Microstruct. **33**, 311 (2003).

[30] M. Gawełczyk, M. Syperek, A. Maryński, P. Mrowiński, Ł. Dusanowski, K. Gawarecki, J. Misiewicz, A. Somers,

J. P. Reithmaier, S. Höfling, and G. Sęk, Exciton lifetime and emission polarization dispersion in strongly in-plane asymmetric nanostructures, Phys. Rev. B **96**, 245425 (2017).

[31] M. Syperek, J. Andrzejewski, E. Rogowicz, J. Misiewicz, S. Bauer, V. I. Sichkovskyi, J. P. Reithmaier, and G. Sęk, Carrier relaxation bottleneck in type-II InAs/InGaAlAs/InP(001) coupled quantum dots-quantum well structure emitting at 1.55 μm, Appl. Phys. Lett. **112**, 221901 (2018).

[32] D. Gammon, E. S. Snow, B. V. Shanabrook, D. S. Katzer, and D. Park, Homogeneous linewidths in the optical spectrum of a single gallium arsenide quantum dot, Science **273**, 87 (1996).

[33] K. Leosson, J. R. Jensen, W. Langbein, and J. M. Hvam, Exciton localization and interface roughness in growth-interrupted GaAs/AlAs quantum wells, Phys. Rev. B **61**, 10322 (2000).

[34] H. D. Robinson, B. B. Goldberg, and J. L. Merz, Observation of excitation transfer among neighboring quantum dots, Phys. Rev. B **64**, 075308 (2001).

[35] A. Babiński, J. Borysiuk, S. Kret, M. Czyż, A. Golnik, S. Raymond, and Z. R. Wasilewski, Natural quantum dots in the InAs/GaAs wetting layer, Appl. Phys. Lett. **92**, 171104 (2008).

[36] G. Sęk, A. Musiał, P. Podemski, M. Syperek, J. Misiewicz, A. Löffler, S. Höfling, L. Worschech, and A. Forchel, Exciton kinetics and few particle effects in self-assembled GaAs-based quantum dashes, J. Appl. Phys. **107**, 096106 (2010).

[37] J. Q. Ning, S. J. Xu, X. Z. Ruan, Y. Ji, H. Z. Zheng, W. D. Sheng, and H. C. Liu, Electronic band structures and electron spins of InAs/GaAs quantum dots induced by wetting-layer fluctuation, J. Appl. Phys. **110**, 054320 (2011).

[38] M. Syperek, M. Baranowski, G. Sęk, J. Misiewicz, A. Löffler, S. Höfling, S. Reitzenstein, M. Kamp, and A. Forchel, Impact of wetting-layer density of states on the carrier relaxation process in low indium content self-assembled (In, Ga)As/GaAs quantum dots, Phys. Rev. B **87**, 125305 (2013).

[39] C. Carmesin, M. Schowalter, M. Lorke, D. Mourad, T. Grieb, K. Müller-Caspary, M. Yacob, J. P. Reithmaier, M. Benyoucef, A. Rosenauer, and F. Jahnke, Interplay of morphology, composition, and optical properties of InP-based quantum dots emitting at the 1.55 μm telecom wavelength, Phys. Rev. B **96**, 235309 (2017).

[40] S. Raymond, S. Studenikin, S.-J. Cheng, M. Pioro-Ladriere, M. Ciorga, P. J. Poole, and M. D. Robertson, Families of islands in InAs/InP self-assembled quantum dots: A census obtained from magneto-photoluminescence, Semicond. Sci. Technol. **18**, 385 (2003).

[41] S. Tomimoto, A. Kurokawa, Y. Sakuma, T. Usuki, and Y. Masumoto, Radiative recombination of excitons in disk-shaped inas/inp quantum dots, Phys. Rev. B **76**, 205317 (2007).

[42] G. Gélinas, A. Lanacer, R. Leonelli, R. A. Masut, and P. J. Poole, Carrier thermal escape in families of InAs/InP self-assembled quantum dots, Phys. Rev. B **81**, 235426 (2010).

[43] F. Guffarth, R. Heitz, A. Schliwa, K. Pötschke, and D. Bimberg, Observation of monolayer-splitting for InAs/GaAs quantum dots, Phys. E Low-Dimens. Syst. Nanostruct. **21**, 326 (2004).

[44] T. S. Kuan, T. F. Kuech, W. I. Wang, and E. L. Wilkie, Long-Range Order in $Al_xGa_{1-x}As$, Phys. Rev. Lett. **54**, 201 (1985).

[45] O. Ueda, T. Fujii, Y. Nakada, H. Yamada, and I. Umebu, TEM investigation of modulated structures and ordered structures in InAlAs crystals grown on (001) InP substrates by molecular beam epitaxy, J. Cryst. Growth **95**, 38 (1989).

[46] W. S. Han, B. Lee, J. H. Baek, J.-H. Lee, B. S. Jung, E.-H. Lee, and O. Byungsung, Ordering effect on band-gap lowering in lattice-matched InAlAs epilayers grown on InP by metal–organic chemical-vapor deposition, Appl. Phys. Lett. **72**, 1905 (1998).

[47] T. S. Kuan, W. I. Wang, and E. L. Wilkie, Long-range order in $In_xGa_{1-x}As$, Appl. Phys. Lett. **51**, 51 (1987).

[48] M. A. Shahid, S. Mahajan, D. E. Laughlin, and H. M. Cox, Atomic Ordering in $Ga_{0.47}In_{0.53}As$ and $Ga_xIn_{1-x}As_yP_{1-y}$ Alloy Semiconductors, Phys. Rev. Lett. **58**, 2567 (1987).

[49] H. R. Jen, K. Y. Ma, and G. B. Stringfellow, Long-range order in InAsSb, Appl. Phys. Lett. **54**, 1154 (1989).

[50] M. A. Shahid and S. Mahajan, Long-range atomic order in $Ga_xIn_{1-x}As_yP_{1-y}$ epitaxial layers [(x, y) = (0.47, 1), (0.37, 0.82), (0.34, 0.71), and (0.27, 0.64)], Phys. Rev. B **38**, 1344 (1988).

[51] M. Ishimaru, S. Matsumura, N. Kuwano, and K. Oki, Kinetics of CuPt-type ordered phase formation in III-V semiconductor alloys during (001) epitaxial growth due to step flow, Phys. Rev. B **51**, 9707 (1995).

[52] K. Kurihara, H. Namita, R. Ueda, M. Takashima, K. Akimoto, K. Sakata, T. Takahashi, T. Nakamura, and K. Shimoyama, Ordering structure along the direction of InAlAs, J. Cryst. Growth **272**, 9 (2004).

[53] D. U. Lee, J. Y. Jin, T. Y. Yun, T. W. Kim, H. S. Lee, M. S. Kwon, and J. Y. Lee, Atomic arrangements of a CuAu-I type ordered structure in strained $In_xGa_{1-x}As/In_yAl_{1-y}As$ multiple quantum wells, J. Mater. Sci. **40**, 3843 (2005).

[54] P. Möck, T. Topuria, N. D. Browning, G. R. Booker, N. J. Mason, R. J. Nicholas, M. Dobrowolska, S. Lee, and J. K. Furdyna, Internal self-ordering in In(Sb, As), (In, Ga)Sb, and (Cd, Zn, Mn)Se nano-agglomerates/quantum dots, Appl. Phys. Lett. **79**, 946 (2001).

[55] A. A. Mbaye, L. G. Ferreira, and A. Zunger, First-Principles Calculation of Semiconductor-Alloy Phase Diagrams, Phys. Rev. Lett. **58**, 49 (1987).

[56] G. P. Srivastava, J. L. Martins, and A. Zunger, Atomic structure and ordering in semiconductor alloys, Phys. Rev. B **31**, 2561 (1985).

[57] T. Suzuki, A. Gomyo, and S. Iijima, Strong ordering in GaInP alloy semiconductors formation mechanism for the ordered phase, J. Cryst. Growth **93**, 396 (1988).

[58] E. T. Jaynes, Information theory and statistical mechanics, Phys. Rev. **106**, 620 (1957).

[59] E. T. Jaynes, Information theory and statistical mechanics. II, Phys. Rev. **108**, 171 (1957).

[60] A. K. Livesey and J. C. Brochon, Analyzing the distribution of decay constants in pulse-fluorimetry using the maximum entropy method, Biophys. J. **52**, 693 (1987).

[61] Y. Varshni, Temperature dependence of the energy gap in semiconductors, Physica **34**, 149 (1967).

[62] M. Baranowski, M. Syperek, R. Kudrawiec, J. Misiewicz, J. A. Gupta, X. Wu, and R. Wang, Carrier dynamics between delocalized and localized states in type-II GaAsSb/GaAs quantum wells, Appl. Phys. Lett. **98**, 061910 (2011).

[63] M. Baranowski, R. Kudrawiec, M. Latkowska, M. Syperek, J. Misiewicz, and J. A. Gupta, Dynamics of localized excitons in $Ga_{0.69}In_{0.31}N_{0.015}As_{0.985}$/GaAs quantum well: Experimental studies and monte-carlo simulations, Appl. Phys. Lett. **100**, 202105 (2012).

[64] W. Lei, Y. Chen, B. Xu, P. Jin, Y. Wang, C. Zhao, and Z. Wang, Anomalous temperature dependence of photoluminescence peak energy in InAs/InAlAs/InP quantum dots, Solid State Commun. **137**, 606 (2006).